Govindarajan *et al.*
Nanoscale Research Letters (2022) 17:65
https://doi.org/10.1186/s11671-022-03704-5

Nanoscale Research Letters

RESEARCH Open Access

Sputter-Deposited Binder-Free Nanopyramidal Cr/γ-Mo_2N TFEs for High-Performance Supercapacitors

Durai Govindarajan[1], Nithyadharseni Palaniyandy[2], Karthik Kumar Chinnakutti[3], Mai Thanh Nguyen[4], Tetsu Yonezawa[4], Jiaqian Qin[5] and Soorathep Kheawhom[1,6,7*]

Abstract

Due to their outstanding power density, long cycle life and low cost, supercapacitors have gained much interest. As for supercapacitor electrodes, molybdenum nitrides show promising potential. Molybdenum nitrides, however, are mainly prepared as nanopowders via a chemical route and require binders for the manufacture of electrodes. Such electrodes can impair the performance of supercapacitors. Herein, binder-free chromium (Cr)-doped molybdenum nitride (Mo_2N) TFEs having different Cr concentrations are prepared via a reactive co-sputtering technique. The Cr-doped Mo_2N films prepared have a cubic phase structure of γ-Mo_2N with a minor shift in the (111) plane. While un-doped Mo_2N films exhibit a spherical morphology, Cr-doped Mo_2N films demonstrate a clear pyramid-like surface morphology. The developed Cr-doped Mo_2N films contain 0–7.9 at.% of Cr in Mo_2N lattice. A supercapacitor using a Cr-doped Mo_2N electrode having the highest concentration of Cr reveals maximum areal capacity of 2780 mC/cm^2, which is much higher than that of an un-doped Mo_2N electrode (110 mC/cm^2). Furthermore, the Cr-doped Mo_2N electrode demonstrates excellent cycling stability, achieving ~ 94.6% capacity retention for about 2000 cycles. The reactive co-sputtering proves to be a suitable technique for fabrication of binder-free TFEs for high-performance energy storage device applications.

Keywords: Molybdenum nitride, Chromium-doped, Co-sputtering, Supercapacitors, Cycling stability

Introduction

Electrochemical capacitors (ECs) or supercapacitors (SCs) are in high demand for a variety of applications, e.g., portable, wearable/flexible devices and electronic industries, as well as electric vehicles (EVs) due to their high-power density, fast charge–discharge and longer cycle life, [1–4]. Because of their enormous surface area, carbon-based materials (EDLC) including activated carbon remain the most used electrode material for ECs. However, carbon-based materials exhibit inferior energy density [5, 6]. Owing to their high capacitance, metal oxides/nitrides (pseudocapacitors) have been explored as alternative electrode materials for batteries and supercapacitors [5–8]. Yet, metal oxides reveal low electrical conductivity, which restricts their capacitance/capacity. There has been an urgent need, therefore, to replace carbon and metal oxide-based electrode materials with high-performance electrode materials [9].

Recently, sulfides and nitride-based materials have shown promise for the development of high-performance electrochemical ECs due to their outstanding electrochemical properties [10–12]. Because of their structural stability, unique physiochemical features, good electrocatalytic activities and superior electrical conductivity, metal nitrides are highly considered electrode material for ECs [12, 13]. So far, nitride-based electrodes, such as TiN [14, 15], VN [16–19], RuN [20], Mo_2N [21–23],

*Correspondence: soorathep.k@chula.ac.th

[1] Department of Chemical Engineering, Faculty of Engineering, Chulalongkorn University, Bangkok 10330, Thailand
Full list of author information is available at the end of the article

Ni_2Mo_3N [24], Ni_3N [25], MnN@rGO [26] and CrN [27–29] electrodes, have been investigated for application in ECs. Molybdenum nitrides have been pursued as a viable electrode material for ECs owing to their great catalytic activity, excellent electrochemical behavior, low compressibility and high melting point. However, molybdenum nitrides as well as other metal nitrides are mainly prepared using chemical synthesis techniques, which result in mechanical instability and significant energy consumption. Moreover, studies of their electrochemical properties are still inadequate [30–32]. Nanomaterials prepared by chemical synthesis techniques in the form of nanopowder are in need of binders such as polyvinylidene fluoride (PVDF), polyvinyl alcohol (PVA) and carboxymethyl cellulose (CMC) to fabricate electrodes. Yet, such binders are known to hinder the performance of electrodes. Therefore, researchers are searching for other synthesis methods without using any binder [10, 25].

Due to the uniformity plus controlled stoichiometry of their coatings, good adhesion and well-defined structure, binder-free nitride-based thin film electrodes (TFEs) prepared by a sputtering technique are noted for producing high-performance, stable and flexible ECs [30]. Of note, the [111] grown molybdenum nitride films grown by using reactive direct current (DC) magnetron sputtering on titanium substrate at 400 °C demonstrate high areal capacitance of 55 mF cm^{-2} and excellent cycling stability of 100% capacitance retention after 2000 cycles [33]. Adalati et al. [34] synthesized a molybdenum and vanadium nitride binder-free thin film on a stainless steel substrate through reactive sputtering technique by varying the sputtering parameters such as Ar/N_2 gas flow, applied DC power and deposition pressure. Vanadium nitride and molybdenum nitride were used to develop an asymmetrical device. These electrodes showed areal capacitances of 82.35 mF cm^{-2} (MoN) and 67.50 mF cm^{-2} (VN), respectively, with a capacitance retention of approximately 95.23%. Shi et al. [35] synthesized intercolumnar porous CrN TFEs at a substrate temperature of 250 °C under various N_2 ratios, which displayed an areal capacitance of 41.7 mF cm^{-2} in H_2SO_4 electrolyte. Gao et al. [36] reported the synthesis of nanoporous CrN containing different ratios of metallic nickel (Ni), viz. 0, 30.4, 54.2 and 77.6 at.% (CrN-Ni) using arc ion plating. The nanoporous coating obtained using 54.2 at.% Ni, containing the CrN-Ni film, exhibited the highest capacitance of 58.5 mF cm^{-2} at 1.0 mA cm^{-2} greater than all other coatings, i.e., much higher than that of the as-deposited CrN electrode. In addition, this binder-free electrode provided an excellent capacitance retention rate. In general, doping of selective metal ions into host materials has proved to be a very good way to increase electrical conductivity and capacitance. However, there is still a gap in the development of binder-free metal nitride-based electrodes. To the best of our knowledge, no report has been published previously on the synthesis of binder-free Cr-doped Mo_2N TFEs (TFEs) material for ECs. Thus, for the first time, novel binder-free Cr-substituted Mo_2N TFEs have been developed for high-efficiency energy storage devices; their improved electrochemical performances are compared with existing metal nitrides-based electrodes.

Cr was chosen as a dopant in this work mainly because it is a metal having good electrical conductivity (0.0774 10^6/cm Ω and 7.9×10^6 S/m) and low ionic radii (0.62 Å). Cr is low in cost compared with other high conductive metals (Ag, Pt, V, Ru Ti and Ni). Besides, Cr is abundant (83% natural abundance) as well as corrosion-resistant. The addition of Cr in Mo_2N synergistically alters the electronic states and creates better attainable active sites, enhancing the electrochemical performance and improving conductivity.

In the present work, nanopyramidal Cr-doped Mo_2N (Cr/Mo_2N) binder-free TFEs with different Cr doping concentrations: 0 to ~ 8 at.%, have been successfully synthesized via a reactive magnetron co-sputtering method for high-performance energy storage devices. Binder-free Mo_2N TFEs show promise as active anode material for ECs. The impact of Cr on Mo_2N as well as the microstructural and electrochemical charge storage properties of binder-free TFEs is discussed.

Experimental Section

Cr-Doped Mo_2N Thin Films Deposition

Cr-doped MoN thin films are synthesized via a reactive co-sputtering technique (MP 300 sputter system, Plassys, France) along with 2 inch Cr and Mo targets having a purity of ~ 99.99% using argon (Ar^+) as sputtering and nitrogen (N_2) as reactive gases. In advance of deposition, the substrates: glass, silicon (100) and stainless steel 304, were cleaned (ultrasonically) by a standard cleaning process using acetone/ethanal and deionized water to eliminate the native oxide layers or any other impurities on the surface of the substrates. Subsequently, the substrates were dried and loaded into a sputtering chamber, as shown in Fig. 1.

After loading the substrates into the sputtering chamber, a base vacuum of 4×10^{-6} mbar was achieved using a turbo-molecular pump. Initially, before conducting deposition, both metallic targets were pre-sputtered in the Ar^+ environment for ~ 10 min to eliminate residual native oxides over the target surfaces. During the growth of the film, a negative charge is applied to the target material (Mo and Cr) to initiate sputtering, which ionizes the working gas of the Ar^+ and N sources. Positively

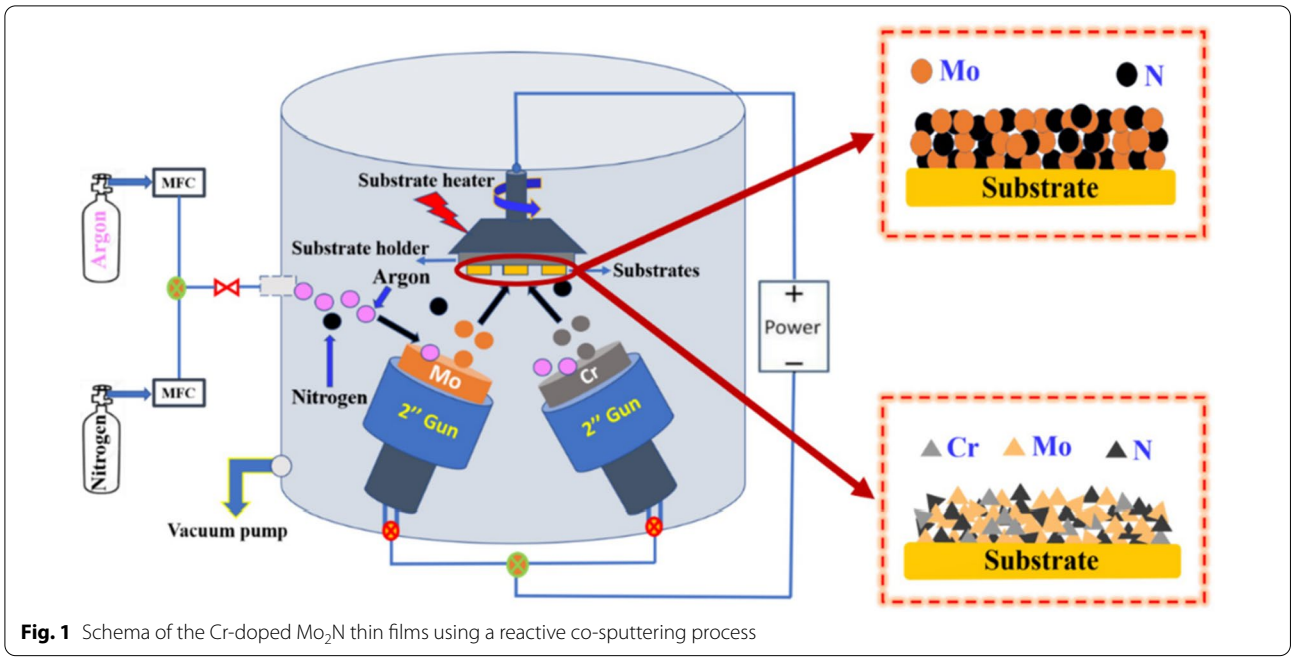

Fig. 1 Schema of the Cr-doped Mo_2N thin films using a reactive co-sputtering process

charged Ar ions, generated in the plasma region, are rapidly attracted to the negatively biased Mo and Cr targets. Consequently, the atomic-sized Mo and Cr particles are ejected from the targets (Mo and Cr) as a result of the collision's momentum transfer. The plasmas negatively charged N_2 atoms react with the Cr and Mo atoms; the resultant Cr/MoN thin film is ultimately deposited on the surface of the substrates. Herein, the Cr atoms introduced bind to the Mo_2N crystal lattice directly through a three-body collision of Cr, Mo and N_2 (Additional file 1: Fig. S1). All the films were prepared at a substrate temperature of 573 K (±5) and working pressure of 9.8 mTorr. The Cr-doped Mo_2N thin films were synthesized by fixing the Mo sputter power and varying Cr target power having a constant Ar/N_2 flow rate. For the deposition of the pure Mo_2N sample preparation, Mo target power remained unchanged. In Table 1, the detailed deposition parameters of this work are given. The undoped Mo_2N denotes the Mo_2N film having 0 at.% of Cr. In addition, Cr/Mo_2N-1, Cr/Mo_2N-2, Cr/Mo_2N-3 and Cr/Mo_2N-4 denote the Cr-doped Mo_2N films containing 3.35, 4.87, 6.21 and 7.90 at.% Cr, respectively.

Table 1 Sputtering parameters for the development of Cr-doped Mo_2N thin films

Sputtering deposition parameters	Range
Sputter targets	Metallic molybdenum (Mo) and chromium (Cr) targets: 99.99% purity
Substrates	Type 304 SS and silicon (100)
Target-to-substrate distance	5–6 cm
Base pressure	4×10^{-6} mbar
Working pressure	9.8 mTorr (1.30×10^{-2} mbar)
Substrate temperature	573 K
Sputtering gas (Ar)	14 sccm
Reactive sputtering gas (N_2)	2 sccm
Mo target power (RF gun)	100 (±2) W
Cr target power (DC gun)	0, 8, 10, 12 and 14 (±2) W (for doping)
Duration of the deposition	60 min

Characterization Techniques

The sputter-deposited Cr-doped Mo_2N thin films were investigated using various characterization techniques. Surface morphology and elemental composition of the Cr-doped Mo_2N films were examined by field emission scanning electron microscope (FE-SEM, Carl Zeiss, Supra 55, Germany) and equipped with energy-dispersive X-ray spectrometer (EDS, Oxford instrumental), respectively. The crystallographic orientation and phase purity of the Cr-doped Mo_2N films were characterized using grazing incidence X-ray diffractometer (XRD, D8 Advance, Bruker, Germany). XRD patterns were recorded at the diffraction angle of $2\theta = 20°–70°$ using the Cu-Kα radiation wavelength ($\lambda = 1.54$ Å). To understand the oxidation states and chemical/electronic configuration of the thin films, X-ray photoelectron spectroscopy (XPS) technique

using a ULVAC-PHI, Inc. (PHI Quantera SXM, USA) with an Al K_α X-ray source was adopted.

Electrochemical Measurements

Electrochemical behavior of the Cr-doped Mo_2N TFEs was assessed using an electrochemical workstation (Biologic, SP-300, France) in a 3-electrode cell configuration in 1 M KOH electrolyte. The as-deposited Mo_2N and Cr-doped Mo_2N films on the stainless steel substrates were directly utilized as working electrodes. Ag/AgCl and platinum wire were used as reference and counter electrodes, respectively. Both cyclic voltammetry (CV) and galvanostatic charge–discharge (GCD) techniques were applied to calculate the areal capacity/capacitance with respect to different scan rates and current densities as well as the stability performance of the TFEs. The electrochemical impedance spectroscopy (EIS) technique was employed to examine the charge transfer mechanism of the film electrodes during electrochemical analysis.

Results and Discussion

Structural Characterization

Phase formation and crystal structure of the Mo_2N and Cr-doped Mo_2N thin films with thicknesses ranging from ~ 900 to 1400 nm (Additional file 1: Fig. S2) were initially investigated by XRD analysis. During XRD analysis, scan limit was fixed in the 2θ range of 20°–80°. In Fig. 2, the XRD patterns of as-deposited Mo_2N and Cr-doped Mo_2N thin films are displayed.

In both the un-doped and Cr-doped Mo_2N thin films, three major diffraction peaks are noticed. Around 37.1°, a strong diffraction peak appeared and two low intensity peaks are observed around 43.1° and 79.2°, indexed to (111), (200) and (222) crystallographic orientations of Mo_2N. All diffraction peaks were found to be well matched with γ-Mo_2N (JCPDS file: PDF # 25-1366) having a cubic crystal system. The intensity of the diffraction peak 37.1° shifted slightly with respect to the higher amount of Cr doping concentration in the Mo_2N film (Fig. 2b), confirming Cr ions in the Mo_2N lattice and a sharp intensity peak at 37.1°, indicating high crystallinity of the prepared thin film samples. In Fig. 2b, the diffraction pattern of Cr-doped Mo_2N, at 2θ around 37.1°, shifted to the right compared to the pristine Mo_2N. Such a shift in the peak confirms the substitution of Cr in the Mo site with the presence of tensile stress in the as-deposited films [37, 38]. The expanding grain size caused tensile stress in the as-developed films, demonstrating a decreased lattice parameter (4.13 Å) relative to bulk Mo_2N. In the as-grown films, the XRD pattern exhibited no peaks corresponding to the metallic Mo or Cr, or any other types of Mo/Cr nitrides. By substituting some of the Mo atoms with Cr, it is noted that Cr is completely in a solid solution with Mo_2N and remains as a cubic structure for the entire Cr dopant concentration in the current investigation. Furthermore, the as-deposited thin films are a pure form of Mo_2N, whereas the Cr-doped Mo_2N films are highly crystalline in nature. No secondary phases were detected in the XRD analyses.

Surface Chemistry Studies

XPS was applied to the pristine Mo_2N and Cr/Mo_2N-4 film samples. The energy-dispersive X-ray spectroscopy technique was used to analyze the bulk composition of coatings. Moreover, the XPS technique can analyze surface chemical states at a depth as far as ~ 5 nm. Figure 3a, b shows the full scan survey spectra of the un-doped Mo_2N and Cr/Mo_2N-4 thin films. In Fig. 3c–g,

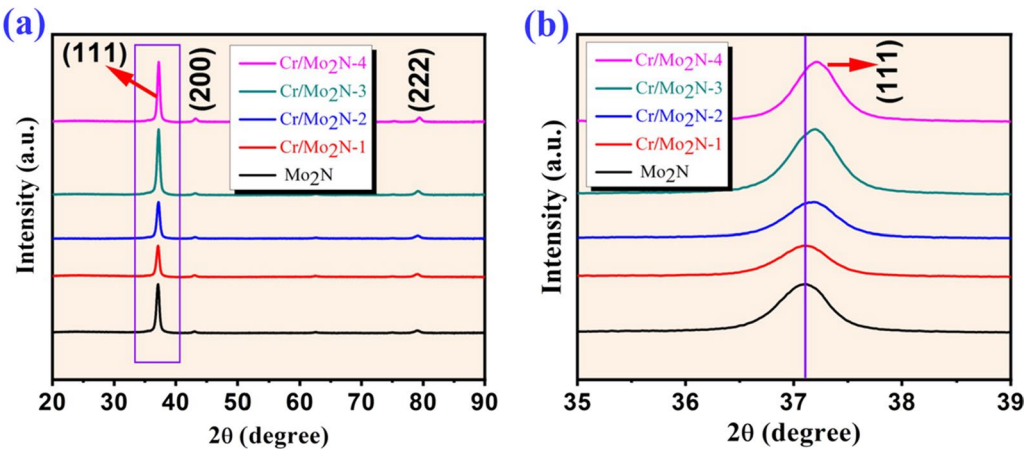

Fig. 2 **a** XRD patterns of Mo_2N and Cr-doped Mo_2N and **b** enlargement of the peak shift of (111) plane with respect to the doping concentration of Cr

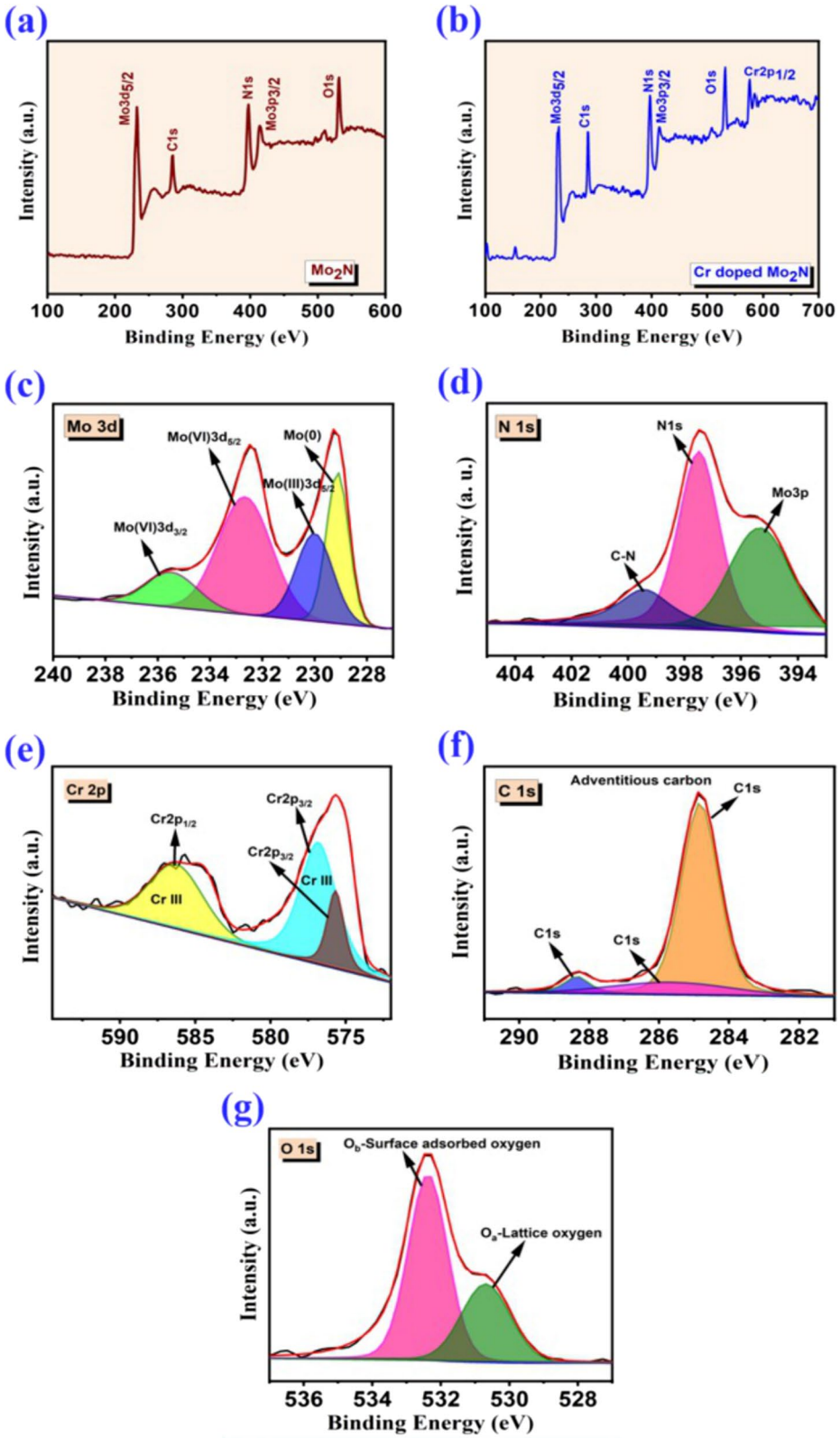

Fig. 3 Schema of XPS spectra: **a** un-doped Mo_2N, **b** Cr-doped Mo_2N thin films, **c** Mo 3*d*, **d** N 1*s*, **e** Cr 2*p*, **f** C 1*s* and **g** O 1*s*

the high-resolution spectra of all the elements present in the thin film samples are displayed. To avoid denitrification of Mo_2N films due to Ar^+ bombardment, no Ar^+ ion etching was done before collecting the X-ray generated electrons. As illustrated in Fig. 3c, the Mo 3d core-level spectrum can be deconvoluted into four peaks, corresponding to Mo^0 (~ 229 eV), Mo^{3+} (~ 230.1 eV) and Mo^{6+} (232.6 and 235.4 eV) species for the Cr–Mo–N film sample. As shown in Fig. 3f, the impure surface of the adventitious carbon (C 1*s*) at binding energy (BE) of 284.8 eV is denoted [39]. In Fig. 3g, the presence of oxide shows that the surface of the Mo species has been oxidized, indicating both lattice oxygen (O_a-530.5 eV) and surface observed oxygen (O_b-532.4 eV), which is mainly due to the contamination by surface oxygen upon exposure to air [40]. Further, two peaks at around 575.7 eV (Cr $2p_{3/2}$) and 586.4 eV (Cr $2p_{1/2}$) are revealed in the Cr-doped Mo_2N thin film samples [41] and ascribed to Mo–Cr, demonstrating that Cr has been incorporated into the Mo_2N host lattice.

In the XPS spectra, tiny peaks at 415 eV (Mo_2N sample, Fig. 3a) and 413.7 eV (Cr/Mo_2N-4 sample, Fig. 3b) are found. Such peaks are associated with the Mo $3p_{3/2}$ region. As shown in Fig. 3a, b, the positions of Mo 3d peaks for Mo–N and Mo–O bonds have shifted somewhat toward the low binding energy area. This behavior can be due to Cr doping, which can lower their bonding energy by sharing the Mo binding connection. In addition, one more primary peak can be detected for both Mo–N and Cr–Mo–N in the N 1*s* XPS spectra; the Mo–N bond is responsible for the peak at 397.4 eV (Fig. 3d). The N 1*s* peak for Cr–Mo–N has shifted to 396.8 eV (397.4 eV for the bare Mo–N), implying that the Cr element has been doped into the Mo_2N lattice by replacing one of the Mo/N elements. In Fig. 3e, the Cr 2*p* XPS spectrum of Cr–Mo–N is seen to have a major peak at 575.7 eV. This peak differs significantly from the 574.2 eV of the Cr metal and the 576.0 eV of Cr, suggesting that the Cr dopants in the Mo–N lattice are Cr ions. In addition, the atomic percentages of the elements present in the thin film samples were roughly calculated from the XPS spectra as follows: Mo-33.18%, N-27.36%, C-15.72%, Cr-9.48% and O-14.26% for the Cr-doped Mo_2N sample and Mo-39.96%, N-33.07%, O-12.39% and C-14.58% for Mo_2N, respectively.

Morphological Studies

Morphological transformation of the pristine Mo_2N and Cr-doped Mo_2N thin films produced by the reactive co-sputtering process was evaluated using FE-SEM analysis. In Fig. 4a–e, FE-SEM images of the un-doped Mo_2N and Cr-doped Mo_2N thin films samples prepared at different concentrations of Cr doping are displayed, respectively. In Fig. 4a, the pure Mo_2N thin film sample exhibits an agglomerated granular microstructure having a smooth surface; average particles are 20–30 nm in size. When doping concentration increases, all Cr/Mo_2N thin film samples signify that the particles are densely packed together and are spread uniformly over the surface (Fig. 4b–e). The FE-SEM images of the Cr-doped Mo_2N samples reveal a triangular pyramidal like surface morphology [42, 43].

Elemental Composition Studies

To examine both the elemental distribution and formation of Mo_2N and Cr-doped Mo_2N thin films, FE-SEM and EDS analyses were carried out. In Fig. 5, EDS reports of the as-prepared thin film samples are depicted. In Fig. 5a, the EDS spectra, viz. the Mo and N signals, can be seen for the un-doped Mo_2N. In Fig. 5b–e, Cr, Mo and N signals are found in the Cr-doped Mo_2N thin films. As Cr doping concentration increased, the intensity of the Cr peak increased**,** confirming the successful formation of the Cr-doped Mo_2N thin films. In Fig. 5, the atomic percentiles for the Cr-doped Mo_2N samples are shown. Besides, the EDS elemental color mapping images of Mo_2N and Cr-doped Mo_2N TFEs are highlighted, which verify the uniform deposition and distribution of Mo and N elements in the Mo_2N thin film sample. Mo, Cr and N elements are all present in the Cr-doped Mo_2N thin film samples (Additional file 1: Fig. S3).

Electrochemical Supercapacitor Performances

Electrochemical performance of the pristine Mo_2N and Cr-doped Mo_2N binder-free TFEs was carried out in 1 M KOH aqueous electrolyte under room temperature in a three-electrode cell setup. The applied voltage window of − 1.2 to − 0.2 V was fixed for both CV and GCD analysis.

Cyclic Voltammetry Analysis

The as-deposited Mo_2N and Cr-doped Mo_2N TFEs were further characterized via CV analysis under different scan rates (20–80 mV/s). Initially, both the stability and reversibility of the electrodes were examined, applying 10 CV cycles at a fixed scan rate of 50 mV/s. In Fig. 6, the CV curves of the bare stainless steel substrate, as-deposited pristine Mo_2N and Cr-doped Mo_2N TFEs are displayed. The shape of the CV curves for all the Cr-doped Mo_2N TFEs is almost similar, and the higher doping concentration of Cr/Mo_2N-4 electrode exhibits the bigger CV area compared to pristine Mo_2N indicating the excellent capacity behavior, outstanding reversibility and rate capability [34]. It is also noted that the CV curves of the metal nitride-based electrodes revealed a quasi-rectangular shape having a superior active surface area

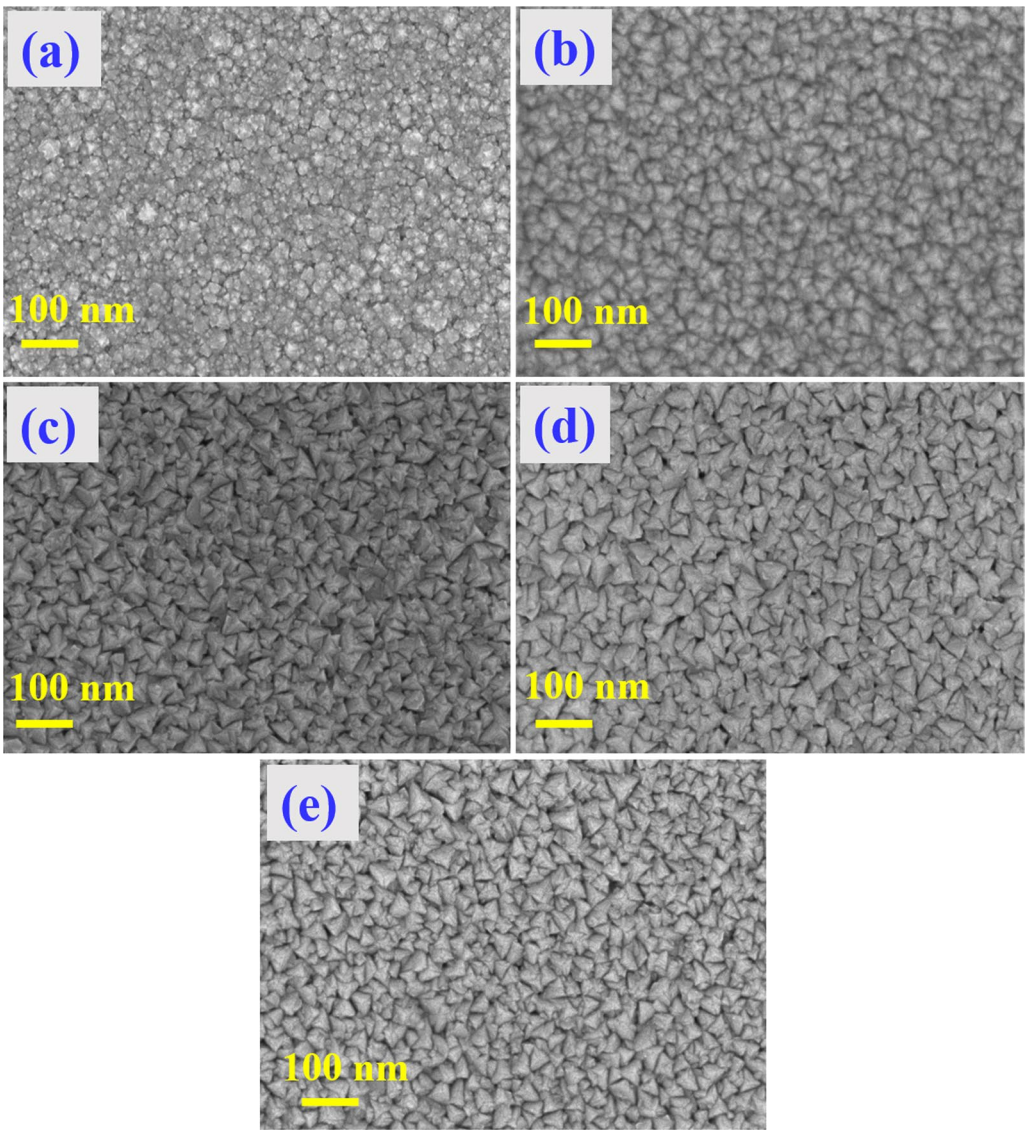

Fig. 4 FE-SEM images: **a** Mo_2N, **b** Cr/Mo_2N-1, **c** Cr/Mo_2N-2, **d** Cr/Mo_2N-3 and **e** Cr/Mo_2N-4 thin films

even at lower scan rates, suggesting excellent charge storage behavior and high-rate capability [44–47]. The areal capacity of the Mo_2N and Cr-doped Mo_2N-based TFEs can be calculated from the CV curves:

$$\text{Areal capacity } (Q_a) = \frac{I}{A \times \nu} \tag{1}$$

where Q_a is the areal capacity (mC/cm^2), I is the current (A), A is the exposed active area of the electrode (cm^2), and ν is the scan rate (mV s^{-1}). Thus, via CV analysis, the maximum areal capacities of Cr/Mo_2N-4 are found to be 2780 mC/cm^2, Cr-doped Mo_2N-3: 2220 mC/cm^2, Cr-doped Mo_2N-2: 1233 mC/cm^2, Cr-doped Mo_2N-1:960 mC/cm^2 at the scan rate of 20 mV/s. The measured areal capacities of the battery-type Cr-doped Mo_2N electrodes are remarkably greater than those of the undoped Mo_2N thin film electrode (110 mC/cm^2), demonstrating the superior charge storage performance of the binder-free electrodes made of other metal nitrides [48, 49]. The increased areal capacity of the grown Cr-doped Mo_2N TFEs may well be caused by the electrolyte ions' increased mobility at the interface between the aqueous electrolyte and active electrode, as well as the synergetic contribution of both Cr and Mo_2N. In Fig. 7a, it is noted that the areal capacity values were found to be substantially greater than those of other metal nitrides-based

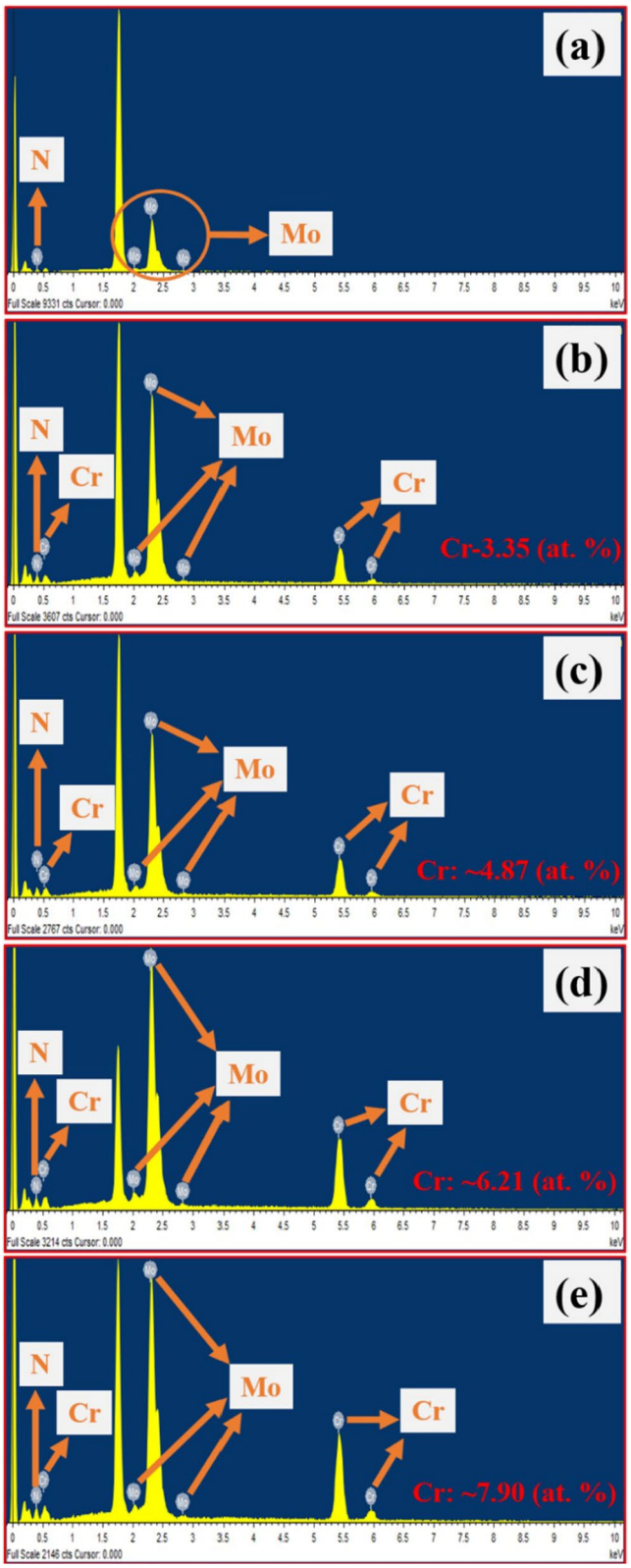

Fig. 5 EDS elemental analysis: **a** Mo_2N, **b** Cr/Mo_2N-1, **c** Cr/Mo_2N-2, **d** Cr/Mo_2N-3 and **e** Cr/Mo_2N-4 thin films

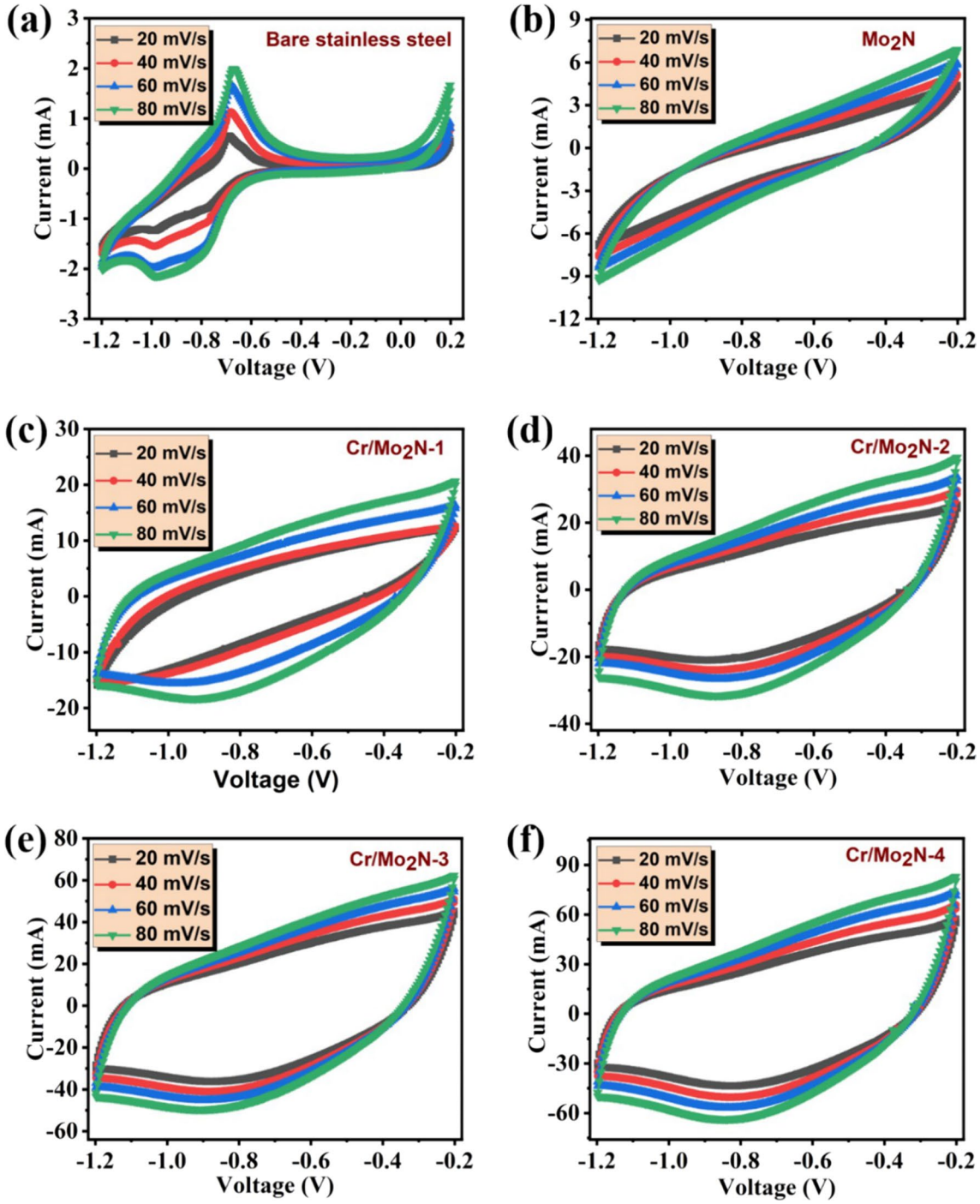

Fig. 6 Cyclic voltammograms: **a** bare stainless steel substrate, **b** as-deposited Mo_2N and **c**–**f** Cr-doped Mo_2N TFEs measured at different scan rates (10–100 mV/s)

electrodes (VN, CrN, TiN, etc.) that had previously been published. In Table 2, the performance of the electrodes are summarized.

Moreover, to better understand the charge storage behavior of Cr-doped Mo_2N TFEs via CV analysis, Dunn's approach is adopted to recognize the two different charge storage contributions: (i) surface-controlled and (ii) diffusion-controlled, which states that the total current at a given potential is the sum of the diffusive and capacitive currents investigated [60]:

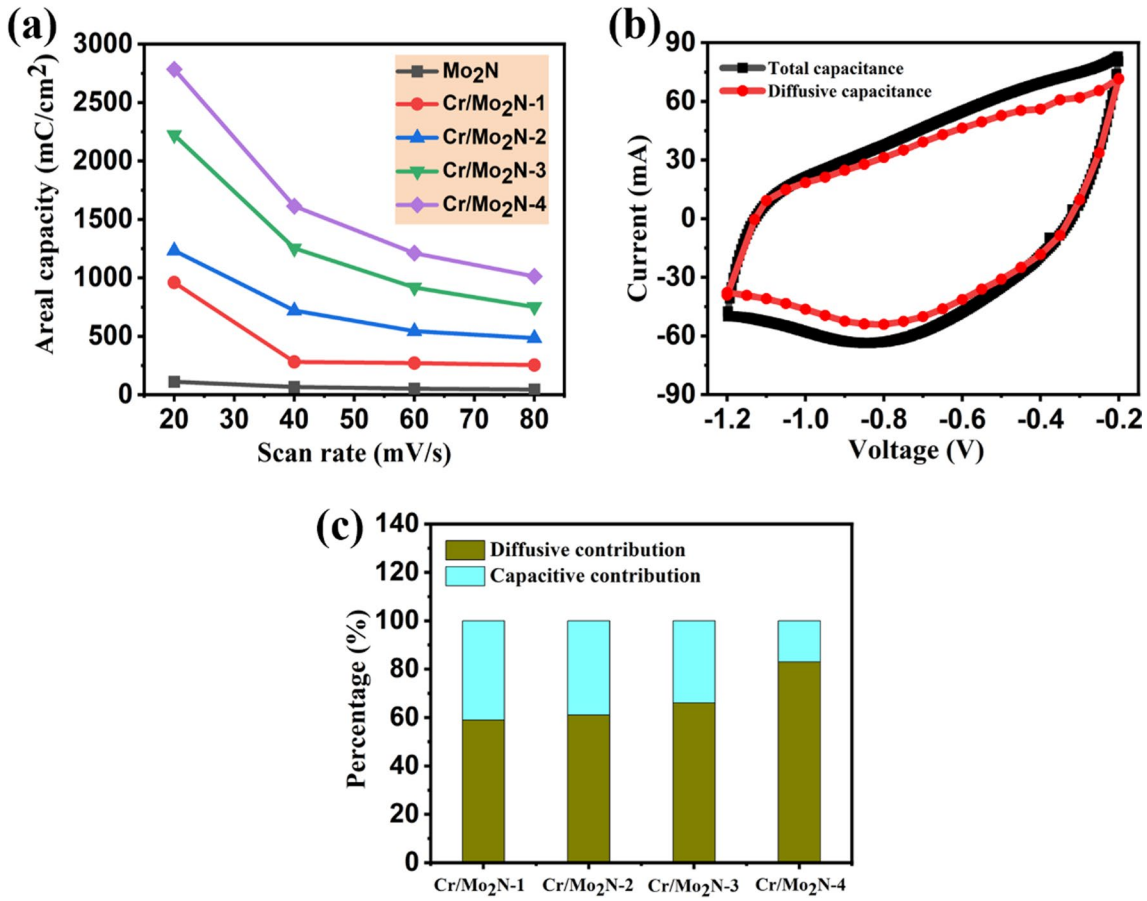

Fig. 7 **a** Areal capacities for the Cr-doped Mo_2N tested under various scan rates, **b** plot of diffusion and capacitive contribution of Cr/Mo_2N-4 electrode evaluated, at a scan rate of 80 mV/s, and **c** illustrating the diffusive and capacitive contributions of different doping concentration of Cr-doped Mo_2N electrodes, at a fixed scan rate of 80 mV/s

$$i(V) = k_1 \nu + k_2 \nu^{0.5} \tag{2}$$

$$i(V)/\nu^{0.5} = k_1 \nu^{0.5} + k_2 \tag{3}$$

where k_1 and k_2 are differentiated as surface- and diffusion-controlled contributions of the developed TFEs, respectively, $i(V)$ is the current of the given potential, ν is the applied scan rate, and k_1 and k_2 values are calculated by plotting the graph between and $i(V)/\nu^{0.5}$ and $(\nu)^{0.5}$. In Fig. 7b, the CV curves of the diffusive and capacitive contribution of the Cr-doped Mo_2N-4 electrode evaluated at a scan rate of 80 mV/s are shown, revealing ~ 83% diffusive contribution to accumulate the charge of the electrode. Besides, the diffusive contribution of Cr/Mo_2N-1, Cr/Mo_2N-2, Cr/Mo_2N-3 and Cr/Mo_2N-4 TFEs is shown to be ~ 83%, ~ 66%, ~ 61% and ~ 59%, respectively (Fig. 7c). These findings suggest that the as-developed nitride-based electrodes have excellent charge storage behavior, with almost mixed contributions (capacitive and diffusive) to total charge storage for lower doping concentrations of Cr in Mo_2N electrodes and the maximum diffusive contribution behavior observed for the higher doping percent of Cr in Mo_2N. As a result, the Cr-doped Mo_2N electrodes are considered to be potential candidates for high-performance energy storage device applications due to the synergetic contribution between Cr dopant and Mo_2N. Additionally, the mechanism of the electrochemical reaction between the active electrode material and the electrolyte can be described as follows:

$$Mo_xN + OH^- \leftrightarrow Mo_xNOH + e^- \tag{4}$$

Galvanostatic Charge–Discharge Analysis

The charge–discharge (CD) performance of the as-prepared electrodes was further examined via GCD studies in 1 M KOH aqueous electrolyte. In Fig. 8a–e, the GCD profiles of Mo_2N and Cr-doped Mo_2N TFEs conducted at different current densities ranging from 1 to 3 mA/cm^2 in a

Table 2 Comparison of the electrochemical performance of Cr-doped Mo_2N film electrodes with other reported metal nitride-based electrode materials

No.	Materials	Synthesis method	Electrolyte	Areal or specific capacitance/capacity	Capacitance/capacity retention with number of cycles	References
1	TiN	Direct current magnetron sputtering	0.5 M K_2SO_4	146.4 F cm^{-3}	–	[15]
2	RuN	Reactive sputtering	1 M $LiPF_6$	37 F/g	–	[20]
3	Ni_2Mo_3N	Ammonolysis synthesis	6 M KOH	264 C/g	81.4%@1000 cycles	[24]
4	Ni_3N	Radio-frequency magnetron sputtering	3 M KOH	319 mF cm^{-2}	93.7%@2000 cycles	[25]
5	γ-Mo_2N	DC sputtering	0.5 M Li_2SO_4	722 F/cm^3	100%@2000 cycles	[33]
6	MoN_x@NF	Atomic layer deposition (ALD)	1 M KOH	130 mC/cm^2	100%@8000	[48]
7	Ni-Co_4N@NC	In situ nitridation process	1 M KOH	397.5 mAh/g	72.4%@10,000 cycles	[50]
8	Mo_3N_2	Reactive magnetron co-sputtering	1 M KOH	173.4 mF cm^2	–	[51]
9	Cu/Mo_3N_2	Reactive magnetron co-sputtering	1 M KOH	619.5 mF cm^2	80%@2000 cycles	[51]
10	Ni-doped Co–Co_2N	Chemical synthesis	1 M KOH	361.93 C/g	82.4%@5000 cycles	[52]
11	W_2N (thick coating)	Sputtering technique	1 M KOH	0.55 F cm^{-2} 700 F cm^{-3}	10,000 cycles	[53]
12	MoN/TiN	Electrodeposition/nitridation treatment in NH_3	1 M LiOH	121.50 mF cm^{-2}	93.8%@1000 cycles	[54]
13	VN	DC plasma reactive sputtering	1 M KOH	238.2 mF cm^{-2}	77.5%@2000 cycles	[55]
14	$Ni_{0.2}Mo_{0.8}N$	Facile and simple nitridation process	6 M KOH	2446 mC/cm^2	80.1%@6000 cycles	[56]
15	Mn_3N_2	Direct current magnetron sputtering	Different electrolytes	118, 68 & 27 mF cm^{-2}	98.5% (KOH), 89% (KCl) and 83% (Na_2SO_4) @4000 cycles	[57]
16	CrN	Direct current magnetron sputtering	0.5 M H_2SO_4	40.53 mF cm^{-2}	95.3%@2000 cycles	[58]
17	CrN	Direct current magnetron sputtering	0.5 M Na_2SO_4	32.69 mF cm^{-2}	93.8%@2000 cycles	[58]
18	CrN	Direct current magnetron sputtering	0.5 M NaCl	9.17 mF cm^{-2}	89.9% 93.8%@2000 cycles	[58]
19	TiN/C	Reactive sputtering	0.5 M H_2SO_4	45.81 mF cm^{-2}	85%@5000 cycles	[59]

fixed voltage window of −1.2 to −0.2 V are presented. In the GCD analysis, the nonlinear shape of the charge–discharge profiles is clearly visible, indicating an ideal capacitive nature; a similar trend of charge–discharge patterns has been seen in previous studies [45, 61]. Hence, the energy storage in the Cr-doped Mo_2N TFEs is attributed to both physisorption of the electric double layer (EDL) and faradaic reaction. The Cr-doped Mo_2N electrode shows a dramatically longer discharging time compared to the pristine Mo_2N electrode, which may account for the substitution of Cr in the Mo_2N lattice. The areal capacity of the TFEs, according to the GCD analysis, is obtained for various current densities and can be expressed as:

$$\text{Areal capacity } (Q_a) = \frac{I \times \Delta t}{A} \tag{5}$$

where Q_a is the areal capacity (mC/cm^2), I is the current (A), Δt is the time difference between the charge/discharge profile (s), and A is the exposure active area of the electrode (cm^2).

Based on the GCD results, the maximum areal capacity of 243 mC/cm^2 for the Cr-doped Mo_2N and 93 mC/cm^2 for the un-doped Mo_2N was attained in 1 mA/cm^2 current density. All the Cr-doped Mo_2N TFEs demonstrated high areal capacities more than the un-doped Mo_2N TFEs (Fig. 8f). These results proved to be much higher than previously reported nitride-based electrodes: CrN [36], Mn_3N_2 [57], Co_3N [62], Nb_4N_5 [63], TiN [64], HfN [65], GaN [66], VN [67] and W_2N [68]. As doping concentration of Cr increased, areal capacity values increased, with respect to various current densities. In Fig. 9f, it is clear that when current density increased, areal capacities decreased, due to insufficient time for complete ion exchange in the electrolyte/electrode interface at higher

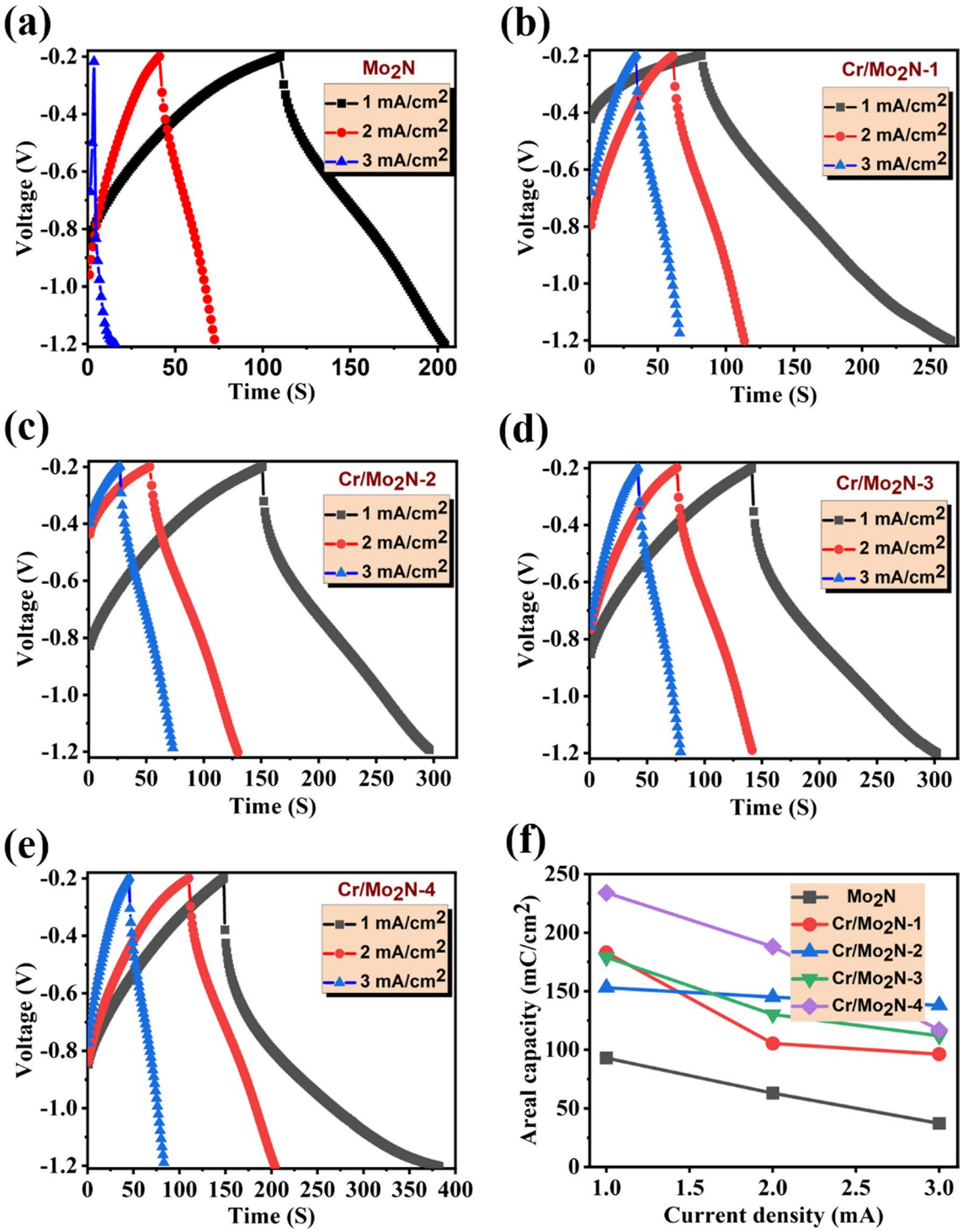

Fig. 8 Charge–discharge profiles: **a** pristine Mo_2N, **b** Cr/Mo_2N-1 TFE, **c** Cr/Mo_2N-2 TFE, **d** Cr/Mo_2N-3 TFE, **e** Cr/Mo_2N-4 TFE and **f** areal capacity with respect to different current densities (1–3 mA/cm^2)

current densities [35]. CD profiles show a curvy and symmetrical linear shape and indicate the superior charge storage behavior of the electrodes having low ohmic potential loss (IR drop), reflecting the great capacity and reversibility of the electrodes [55, 69]. Such positive CD characteristics arose owing to the synergistic effect of

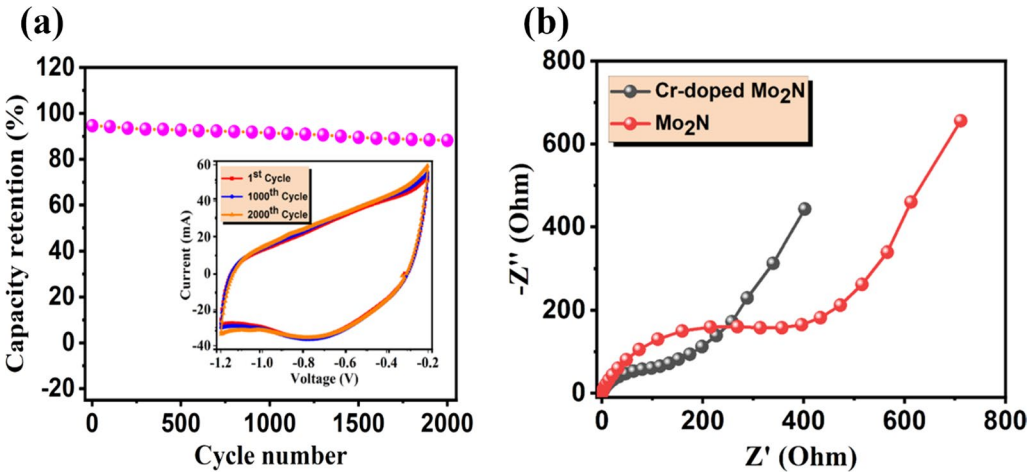

Fig. 9 **a** Cycling performance of Cr-doped Mo_2N-4 thin film electrode performed at 60 mV/s for 2000 cycles (inset: depicting the CV curves of 1st, 1000th and 2000th cycles) and **b** Nyquist plot of un-doped and Cr-doped Mo_2N TFEs

doping Cr with the Mo_2N electrode. The high-efficiency behavior of the as-prepared Cr-doped Mo_2N thin film-based electrodes verifies their potential for use as high-performance ECs.

Cycling Stability and Impedance Analysis

Cycling behavior and rate performance are essential parameters for the practical application of energy storage devices. In Fig. 9a, the Cr/Mo_2-4 electrode measured up to 2000 CV cycles, demonstrating maximum capacity retention of ~ 94.6%. As the number of cycles increased (up to 2000), the rate capability of the electrodes is seen to decrease slowly, which indicates that the prepared nitride-based electrodes are long-lasting even at higher cycles: significantly higher than previously studied metal nitrides such as Nb_4N_5 [46], VN [70] and TiN [71]. It is acknowledged that the improved electrochemical performance of the Cr-doped Mo_2N electrodes can be attributed to the synergistic effect between the dopant and host materials.

Finally, to understand electrochemical kinetics such as the charge transfer process between as-prepared nitride-based electrodes and electrolyte interface, EIS studies were carried out. In Fig. 9b, it is found that the Nyquist plot of Mo_2N and Cr-doped Mo_2N TFEs performed at a frequency range of 1 Hz–100 MHz with an amplitude of 10 mV. According to the electrochemical Nyquist plot, the curve can be separated into three components: electrolyte resistance, a vertical line in the low-frequency zone and a semicircle in the high-frequency zone. The electrolyte resistance, namely the ionic resistance of the electrolyte, intrinsic resistance of the electrode and interface resistance, is represented by the intersection with the x-coordinate in the high-frequency region [72]. The vertical/inclined line in the low-frequency zone of as-prepared nitride-based electrodes is due to the diffusion of ions at the electrode–electrolyte interface, indicating the remarkable conductive behavior of the electrode [34]. The semicircle in the high-frequency zone represents charge transfer resistance (R_{ct}) in the electrode and electrolyte interface along with the R_{ct} of 521 Ω for the un-doped Mo_2N sample and 130 Ω for the Cr-doped Mo_2N thin film sample. During the electrochemical process, the decrease in charge transfer resistance after doping Mo_2N with Cr may be due to rapid electron and ion transfer and excellent electrolyte accessibility. Such an outcome demonstrates that the Cr-doped Mo_2N TFEs can increase the electrode reaction kinetics of binder-free ECs.

Conclusions

In summary, the nanopyramidal-shaped Cr-doped Mo_2N binder-free TFEs were prepared via a reactive co-sputtering technique; their microstructural and electrochemical energy storage properties were systematically elucidated. It is significant that the doping effect of the Cr transition metal played an important role in enhancing the electrochemical energy storage performance of the Mo_2N TFEs. The obtained un-doped and Cr-doped Mo_2N thin films were investigated in detail via XRD, XPS, FE-SEM with EDS analyses. CV studies demonstrated that the ~ 7.9 at.% Cr-doped Mo_2N TFE exhibited a maximum areal capacity of 2780 mC/cm^2, which proved to be much greater than the pristine Mo_2N electrode and other nitride-based TFEs shown in prior investigations. Furthermore, the GCD study demonstrated that the charge–discharge profiles have a symmetrical linear

shape, exhibiting outstanding discharge behavior, with a areal capacity of 243 mC/cm^2. The higher doping concentration of Cr-doped Mo_2N electrode displayed outstanding cycling stability, with a capacity loss of only 5.4% after 2000 CV cycles. The nitride-based TFEs prepared by the reactive co-sputtering technique were found to be a simple technique for developing high-performance binder-free electrodes that proved to have excellent cycling stability, displaying superior electrochemical characteristics for highly valued future energy storage devices.

Supplementary Information

The online version contains supplementary material available at https://doi.org/10.1186/s11671-022-03704-5.

Additional file 1. Growth mechanism of Cr doped Mo_2N TFEs through sputtering technique; FESEM and EDS mapping of TFEs.

Acknowledgements
The Energy Storage Cluster, Chulalongkorn University, is acknowledged.

Author contributions
DG contributed to conceptualization; investigation; data curation; formal analysis; writing—original draft; and writing—review and editing. NP, KKC, MTN, TY and JQ equally contributed to formal analysis and writing—review and editing. SK was involved in formal analysis; funding acquisition; supervision; writing—original draft; and writing—review and editing. All authors read and approved the final manuscript.

Funding
This work was supported by The Program Unit for Human Resources & Institutional Development, Research and Innovation (B16F640166, B05F640153); Chulalongkorn Academic Advancement into its 2nd Century Project for Postdoctoral Fellowship (C2F); Hokkaido University and Accelerating Social Implementation for SDGs Achievement (B) (aXis) from Japan Science and Technology Agency; and Grant-in-Aid for Scientific Research in Priority Area (21H00138 and 19H05162).

Availability of Data and Materials
The datasets used and/or analyzed during the current study are available from the corresponding author on reasonable request.

Declarations

Ethics Approval and Consent to Participate
Not applicable.

Consent for Publication
Not applicable.

Competing Interests
The authors declare that they have no known competing financial interests or personal relationships that could have appeared to influence the work reported in this paper.

Author details
[1]Department of Chemical Engineering, Faculty of Engineering, Chulalongkorn University, Bangkok 10330, Thailand. [2]Institute for the Development of Energy for African Sustainability, College of Engineering, Science and Technology, University of South Africa, Florida Science Campus, Roodepoort 1709, South Africa. [3]Department of Chemistry, Vinayaka Mission's Kirupananda Variyar Arts and Science College, Vinayaka Mission's Research Foundation (Deemed to be University), 636308, Salem, India. [4]Division of Materials Science and Engineering, Faculty of Engineering, Hokkaido University, Hokkaido 060-8628, Japan. [5]Metallurgy and Materials Science Research Institute, Chulalongkorn University, Bangkok 10330, Thailand. [6]Center of Excellence on Advanced Materials for Energy Storage, Chulalongkorn University, Bangkok 10330, Thailand. [7]Bio-Circular-Green-economy Technology & Engineering Center (BCGeTEC), Faculty of Engineering, Chulalongkorn University, Bangkok 10330, Thailand.

Received: 8 June 2022 Accepted: 17 July 2022
Published online: 19 July 2022

References

1. Kang L, Zhang M, Zhang J, Liu S, Zhang N, Yao W, Ye Y, Luo C, Gong Z, Wang C, Zhou X (2020) Dual-defect surface engineering of bimetallic sulfide nanotubes towards flexible asymmetric solid-state supercapacitors. J Mater Chem A 8(45):24053–24064. https://doi.org/10.1039/D0TA08979F
2. Liu S, Kang L, Zhang J, Jung E, Lee S, Jun SC (2020) Structural engineering and surface modification of MOF-derived cobalt-based hybrid nanosheets for flexible solid-state supercapacitors. Energy Storage Mater 1(32):167–177. https://doi.org/10.1016/j.ensm.2020.07.017
3. Liu S, Kang L, Hu J, Jung E, Henzie J, Alowasheeir A, Zhang J, Miao L, Yamauchi Y, Jun SC (2022) Realizing superior redox kinetics of hollow bimetallic bulfide nanoarchitectures by defect-induced manipulation toward flexible solid-state supercapacitors. Small 18(5):2104507. https://doi.org/10.1002/smll.202104507
4. Sahoo S, Ratha S, Rout CS, Nayak SK (2022) Self-charging supercapacitors for smart electronic devices: a concise review on the recent trends and future sustainability. J Mater Sci 57:1–42. https://doi.org/10.1007/s10853-022-06875-9
5. Patra A, Namsheer K, Jose JR, Sahoo S, Chakraborty B, Rout CS (2021) Understanding the charge storage mechanism of supercapacitors: in situ/operando spectroscopic approaches and theoretical investigations. J Mater Chem A 9(46):25852–25891. https://doi.org/10.1039/D1TA07401F
6. Wang G, Zhang L, Zhang J (2012) A review of electrode materials for electrochemical supercapacitors. Chem Soc Rev 41(2):797–828. https://doi.org/10.1039/C1CS15060J
7. Liu S, Kang L, Hu J, Jung E, Zhang J, Jun SC, Yamauchi Y (2021) Unlocking the potential of oxygen-deficient copper-doped Co_3O_4 nanocrystals confined in carbon as an advanced electrode for flexible solid-state supercapacitors. ACS Energy Lett 6(9):3011–3019. https://doi.org/10.1021/acsenergylett.1c01373
8. Kandasamy M, Sahoo S, Nayak SK, Chakraborty B, Rout CS (2021) Recent advances in engineered metal oxide nanostructures for supercapacitor applications: experimental and theoretical aspects. J Mater Chem A 9(33):17643–17700. https://doi.org/10.1039/D1TA03857E
9. Pramitha A, Raviprakash Y (2022) Recent developments and viable approaches for high-performance supercapacitors using transition metal-based electrode materials. J Energy Storage 49:104120. https://doi.org/10.1016/j.est.2022.104120
10. Sahoo S, Krishnamoorthy K, Pazhamalai P, Kim SJ (2018) Copper molybdenum sulfide anchored nickel foam: a high performance, binder-free, negative electrode for supercapacitors. Nanoscale 10(29):13883–13888. https://doi.org/10.1039/C8NR03998D
11. Sahoo S, Naik KK, Late DJ, Rout CS (2017) Electrochemical synthesis of a ternary transition metal sulfide nanosheets on nickel foam and energy storage application. J Alloys Compd 695:154–161. https://doi.org/10.1016/j.jallcom.2016.10.163
12. Zhou Y, Guo W, Li T (2019) A review on transition metal nitrides as electrode materials for supercapacitors. Ceram Int 45(17):21062–21076. https://doi.org/10.1016/j.ceramint.2019.07.151
13. Pallavolu MR, Anil Kumar Y, Nallapureddy RR, Goli HR, Narayan Banerjee A, Joo SW (2022) In situ design of porous vanadium nitride@carbon nanobelts: a promising material for high-performance asymmetric supercapacitors. Appl Surf Sci 575:151734. https://doi.org/10.1016/j.apsusc.2021.151734
14. Achour A, Ducros JB, Porto RL, Boujtita M, Gautron E, Le Brizoual L et al (2014) Hierarchical nanocomposite electrodes based on titanium nitride and carbon nanotubes for micro-supercapacitors. Nano Energy 7:104–113. https://doi.org/10.1016/j.nanoen.2014.04.008

15. Achour A, Porto RL, Soussou M-A, Islam M, Boujtita M, Aissa KA et al (2015) Titanium nitride films for micro-supercapacitors: effect of surface chemistry and film morphology on the capacitance. J Power Sources 300:525–532. https://doi.org/10.1016/j.jpowsour.2015.09.012
16. Yan Y, Li B, Guo W, Pang H, Xue H (2016) Vanadium based materials as electrode materials for high performance supercapacitors. J Power Sources 329:148–169. https://doi.org/10.1016/j.jpowsour.2016.08.039
17. Glushenkov AM, Hulicova-Jurcakova D, Llewellyn D, Lu GQ, Chen Y (2010) Structure and capacitive properties of porous nanocrystalline VN prepared by temperature-programmed ammonia reduction of V_2O_5. Chem Mater 22(3):914–921. https://doi.org/10.1021/cm901729x
18. Bondarchuk O, Morel A, Bélanger D, Goikolea E, Brousse T, Mysyk R (2016) Thin films of pure vanadium nitride: evidence for anomalous non-faradaic capacitance. J Power Sources 324:439–446. https://doi.org/10.1016/j.jpowsour.2016.05.093
19. Morel A, Borjon-Piron Y, Porto RL, Brousse T, Bélanger D (2016) Suitable conditions for the use of vanadium nitride as an electrode for electrochemical capacitor. J Electrochem Soc 163(6):A1077–A1082. https://doi.org/10.1149/2.1221606jes
20. Bouhtiyya S, Lucio Porto R, Laïk B, Boulet P, Capon F, Pereira-Ramos JP et al (2013) Application of sputtered ruthenium nitride thin films as electrode material for energy-storage devices. Scr Mater 68(9):659–662. https://doi.org/10.1016/j.scriptamat.2013.01.030
21. Dubal DP, Abdel-Azeim S, Chodankar NR, Han Y-K (2019) Molybdenum nitride nanocrystals anchored on phosphorus-incorporated carbon fabric as a negative electrode for high-performance asymmetric pseudocapacitor. IScience 16:50–62. https://doi.org/10.1016/j.isci.2019.05.018
22. Shah SIU, Hector AL, Owen JR (2014) Redox supercapacitor performance of nanocrystalline molybdenum nitrides obtained by ammonolysis of chloride- and amide-derived precursors. J Power Sources 266:456–463. https://doi.org/10.1016/j.jpowsour.2014.05.045
23. Xiong Z, Yang J, Gao Z, Yang Q, Shi D (2020) Orthorhombic Mo_3N_2 nanobelts with improved electrochemical properties as electrode material for supercapacitors. Results Phys 16:102941. https://doi.org/10.1016/j.rinp.2020.102941
24. Kumar R, Bhuvana T, Sharma A (2020) Ammonolysis synthesis of nickel molybdenum nitride nanostructures for high-performance asymmetric supercapacitors. New J Chem 44(33):14067–14074. https://doi.org/10.1039/D0NJ01693D
25. Prasad S, Durai G, Devaraj D, AlSalhi MS, Theerthagiri J, Arunachalam P et al (2018) 3D nanorhombus nickel nitride as stable and cost-effective counter electrodes for dye-sensitized solar cells and supercapacitor applications. RSC Adv 8(16):8828–8835. https://doi.org/10.1039/C8RA00347E
26. Sridhar V, Park H (2019) Manganese nitride stabilized on reduced graphene oxide substrate for high performance sodium ion batteries, super-capacitors and EMI shielding. J Alloys Compd 808:151748. https://doi.org/10.1016/j.jallcom.2019.151748
27. Guerra A, Haye E, Achour A, Harnois M, Hadjersi T, Colomer JF, Pireaux JJ, Lucas S, Boukherroub R (2019) High performance of 3D silicon nanowires array@CrN for electrochemical capacitors. Nanotechnology 31(3):035407. https://doi.org/10.1088/1361-6528/ab4963
28. Wei B, Liang H, Zhang D, Wu Z, Qi Z, Wang Z (2017) CrN thin films prepared by reactive DC magnetron sputtering for symmetric supercapacitors. J Mater Chem A 5(6):2844–2851. https://doi.org/10.1039/C6TA09985H
29. Haye E, Achour A, Guerra A, Moulaï F, Hadjersi T, Boukherroub R, Panepinto A, Brousse T, Pireaux JJ, Lucas S (2019) Achieving on chip micro-supercapacitors based on CrN deposited by bipolar magnetron sputtering at glancing angle. Electrochim Acta 324:134890. https://doi.org/10.1016/j.electacta.2019.134890
30. Zhong Y, Xia X, Shi F, Zhan J, Tu J, Fan HJ (2016) Transition metal carbides and nitrides in energy storage and conversion. Adv Sci 3(5):1500286. https://doi.org/10.1002/advs.201500286
31. Kang Y, Deng C, Chen Y, Liu X, Liang Z, Li T, Hu Q, Zhao Y (2020) Binder-free electrodes and their application for Li-ion batteries. Nanoscale Res Lett 15(1):1–9. https://doi.org/10.1186/s11671-020-03325-w
32. Gerard O, Numan A, Krishnan S, Khalid M, Subramaniam R, Kasi R (2022) A review on the recent advances in binder-free electrodes for electrochemical energy storage application. J Energy Storage 50:104283. https://doi.org/10.1016/j.est.2022.104283
33. Chen L, Liu C, Zhang Z (2017) Novel [111] oriented γ-Mo_2N thin films deposited by magnetron sputtering as an anode for aqueous micro-supercapacitors. Electrochim Acta 245:237–248. https://doi.org/10.1016/j.electacta.2017.05.102
34. Adalati R, Kumar A, Kumar Y, Chandra RA (2020) High-performing asymmetric supercapacitor of molybdenum nitride and vanadium nitride thin films as binder-free electrode grown through reactive sputtering. Energy Technol 8(10):2000466. https://doi.org/10.1002/ente.202000466.35
35. Shi J, Jiang B, Li C, Yan F, Wang D, Yang C, Wang X, Liu Z (2021) Sputtered chromium nitride films with finely tuned intra-and intercolumnar porosities as pseudocapacitive electrode for supercapacitors. Surf Coat Technol 405:126535. https://doi.org/10.1016/j.surfcoat.2020.126535
36. Gao Z, Wan Z, Wu Z, Huang X, Li H, Zhang TF et al (2021) Synthesis and electrochemical properties of nanoporous CrN thin film electrodes for supercapacitor applications. Mater Des 209:109949. https://doi.org/10.1016/j.matdes.2021.109949
37. ul Haq M, Zhang Z, Wen Z, Khan S, ud Din S, Rahman N et al (2019) Humidity sensor based on mesoporous Al-doped NiO ultralong nanowires with enhanced ethanol sensing performance. J Mater Sci Mater 30(7):7121–7134. https://doi.org/10.1007/s10854-019-01030-8
38. Irum S, Andleeb S, Sardar S, Mustafa Z, Ghaffar G, Mumtaz M et al (2021) Chemical synthesis and antipseudomonal activity of Al-doped NiO nanoparticles. Front Mater 8:673458. https://doi.org/10.3389/fmats.2021.673458
39. Greczynski G, Hultman L (2020) X-ray photoelectron spectroscopy: towards reliable binding energy referencing. Prog Mater Sci 107:100591. https://doi.org/10.1016/j.pmatsci.2019.100591
40. Huang Y, Ge J, Hu J, Zhang J, Hao J, Wei Y (2018) Nitrogen-doped porous molybdenum carbide and phosphide hybrids on a carbon matrix as highly effective electrocatalysts for the hydrogen evolution reaction. Adv Energy Mater 8(6):1701601. https://doi.org/10.1002/aenm.201701601
41. Zhao W, DiSalvo FJ (2015) Direct access to macroporous chromium nitride and chromium titanium nitride with inverse opal structure. Chem Commun 51(23):4876–4879. https://doi.org/10.1039/C4CC09564B
42. Kumar A, Sanger A, Kumar A, Chandra R (2017) Single-step growth of pyramidally textured NiO nanostructures with improved supercapacitive properties. Int J Hydrog Energy 42(9):6080–6087. https://doi.org/10.1016/j.ijhydene.2016.11.036
43. Qi Z, Wei B, Wang J, Yang Y, Wang Z (2019) Nanostructured porous CrN thin films by oblique angle magnetron sputtering for symmetric supercapacitors. J Alloys Compd 806:953–959. https://doi.org/10.1016/j.jallcom.2019.07.325
44. Su H, Xiong T, Tan Q, Yang F, Appadurai PBS, Afuwape AA et al (2020) Asymmetric pseudocapacitors based on interfacial engineering of vanadium nitride hybrids. Nanomaterials 10(6):1141. https://doi.org/10.3390/nano10061141
45. Hassan M, Gondal MA, Cevik E, Qahtan TF, Bozkurt A, Dastageer MA (2020) High performance pliable supercapacitor fabricated using activated carbon nanospheres intercalated into boron nitride nanoplates by pulsed laser ablation technique. Arab J Chem 13(8):6696–6707. https://doi.org/10.1016/j.arabjc.2020.06.024
46. Cui H, Zhu G, Liu X, Liu F, Xie Y, Yang C et al (2015) Niobium nitride Nb4N5 as a new high-performance electrode material for supercapacitors. Adv Sci 2(12):1500126. https://doi.org/10.1002/advs.201500126
47. Li X-S, Xu M-M, Yang Y, Huang Q-B, Wang X-Y, Ren J-L et al (2019) MnO_2@Corncob carbon composite electrode and all-solid-state supercapacitor with improved electrochemical performance. Materials 12(15):2379. https://doi.org/10.3390/ma12152379
48. Nandi DK, Sahoo S, Kim TH, Cheon T, Sinha S, Rahul R, Jang Y, Bae JS, Heo J, Shim JJ, Kim SH (2018) Low temperature atomic layer deposited molybdenum nitride–Ni–foam composite: an electrode for efficient charge storage. Electrochem Commun 1(93):114–118. https://doi.org/10.1016/j.elecom.2018.07.003
49. Simon P, Gogotsi Y, Dunn B (2014) Where do batteries end and supercapacitors begin? Science 343(6176):1210–1211. https://doi.org/10.1126/science.1249625
50. Shinde PA, Chodankar NR, Abdelkareem MA, Han YK, Olabi AG (2022) Nitridation-induced in situ coupling of Ni-Co_4N particles in nitrogen-doped carbon nanosheets for hybrid supercapacitors. Chem Eng J 428:131888. https://doi.org/10.1016/j.cej.2021.131888

51. Durai G, Kuppusami P, Theerthagiri J (2018) Microstructural and supercapacitive properties of reactive magnetron co-sputtered Mo_3N_2 electrodes: effects of Cu doping. Mater Lett 220:201–204. https://doi.org/10.1016/j.matlet.2018.02.120
52. Liu X, Zang W, Guan C, Zhang L, Qian Y, Elshahawy AM, Zhao D, Pennycook SJ, Wang J (2018) Ni-doped cobalt–cobalt nitride heterostructure arrays for high-power supercapacitors. ACS Energy Lett 3(10):2462–2469. https://doi.org/10.1021/acsenergylett.8b01393
53. Ouendi S, Robert K, Stiévenard D, Brousse T, Roussel P, Lethien C (2019) Sputtered tungsten nitride films as pseudocapacitive electrode for on chip micro-supercapacitors. Energy Storage Mater 20:243–252. https://doi.org/10.1016/j.ensm.2019.04.006
54. Xie Y, Tian F (2017) Capacitive performance of molybdenum nitride/titanium nitride nanotube array for supercapacitor. Mater Sci Eng B 215:64–70. https://doi.org/10.1016/j.mseb.2016.11.005
55. Achour A, Lucio-Porto R, Solaymani S, Islam M, Ahmad I, Brousse T (2018) Reactive sputtering of vanadium nitride thin films as pseudo-capacitor electrodes for high areal capacitance and cyclic stability. J Mater Sci Mater 29(15):13125–13131. https://doi.org/10.1007/s10854-018-9435-z
56. Ruan Y, Lv L, Li Z, Wang C, Jiang J (2017) Ni nanoparticles@Ni–Mo nitride nanorod arrays: a novel 3D-network hierarchical structure for high areal capacitance hybrid supercapacitors. Nanoscale 9(45):18032–18041. https://doi.org/10.1039/C7NR05560A
57. Durai G, Kuppusami P, Maiyalagan T, Ahila M, Vinoth Kumar P (2019) Supercapacitive properties of manganese nitride thin film electrodes prepared by reactive magnetron sputtering: effect of different electrolytes. Ceram Int 45(14):17120–17127. https://doi.org/10.1016/j.ceramint.2019.05.265
58. Shi J, Jiang B, Liu Z, Li C, Yan F, Liu X et al (2021) Effects of specific surface area of electrode and different electrolyte on capacitance properties in nano porous-structure CrN thin film electrode for supercapacitor. Ceram Int 47(13):18540–18549. https://doi.org/10.1016/j.ceramint.2021.03.177
59. Shi J, Jiang B, Li C, Liu Z, Yan F, Liu X et al (2022) Study on capacitance properties of the sputtered carbon doped titanium nitride electrode material for supercapacitor. Vacuum 198:110893. https://doi.org/10.1016/j.vacuum.2022.110893
60. Augustyn V, Simon P, Dunn B (2014) Pseudocapacitive oxide materials for high-rate electrochemical energy storage. Energy Environ Sci 7(5):1597–1614. https://doi.org/10.1039/C3EE44164D
61. Majumder M, Choudhary RB, Thakur AK, Karbhal I (2017) Impact of rare-earth metal oxide (Eu_2O_3) on the electrochemical properties of a polypyrrole/CuO polymeric composite for supercapacitor applications. RSC Adv 7:20037–20048. https://doi.org/10.1039/C7RA01438D
62. Zhang H, Hu W, Wei B, Zheng J, Qi Z, Wang Z (2021) Freestanding Co_3N thin film for high performance supercapacitors. Ceram Int 47(3):3267–3271. https://doi.org/10.1016/j.ceramint.2020.09.166
63. Gao B, Xiao X, Su J, Zhang X, Peng X, Fu J et al (2016) Synthesis of mesoporous niobium nitride nanobelt arrays and their capacitive properties. Appl Surf Sci 383:57–63. https://doi.org/10.1016/j.apsusc.2016.04.173
64. Wang H-Y, Li B, Teng J-X, Zhu H-L, Qi Y-X, Yin L-W et al (2017) N-doped carbon-coated TiN exhibiting excellent electrochemical performance for supercapacitors. Electrochim Acta 257:56–63. https://doi.org/10.1016/j.electacta.2017.10.066
65. Gao Z, Wu Z, Zhao S, Zhang T, Wang Q (2019) Enhanced capacitive property of HfN film electrode by plasma etching for supercapacitors. Mater Lett 235:148–152. https://doi.org/10.1016/j.matlet.2018.10.032
66. Wang S, Zhang L, Sun C, Shao Y, Wu Y, Lv J et al (2016) Gallium nitride crystals: novel supercapacitor electrode materials. Adv Mater 28(19):3768–3776. https://doi.org/10.1002/adma.201600725
67. Durai G, Kuppusami P, Maiyalagan T, Theerthagiri J, Vinoth Kumar P, Kim H-S (2019) Influence of chromium content on microstructural and electrochemical supercapacitive properties of vanadium nitride thin films developed by reactive magnetron co-sputtering process. Ceram Int 45(10):12643–12653. https://doi.org/10.1016/j.ceramint.2019.02.170
68. Prakash R, Kumar A, Pandey A, Kaur D (2019) Binder free and high performance of sputtered tungsten nitride thin film electrode for supercapacitor device. Int J Hydrog Energy 44(21):10823–10832. https://doi.org/10.1016/j.ijhydene.2019.02.005
69. Lang X-Y, Liu B-T, Shi X-M, Li Y-Q, Wen Z, Jiang Q (2016) Ultrahigh-power pseudocapacitors based on ordered porous heterostructures of electron-correlated oxides. Adv Sci 3(5):1500319. https://doi.org/10.1002/advs.201500319
70. Wang Y, Jiang M, Yang Y, Ran F (2016) Hybrid electrode material of vanadium nitride and carbon fiber with cigarette butt/metal ions wastes as the precursor for supercapacitors. Electrochim Acta 222:1914–1921. https://doi.org/10.1016/j.electacta.2016.12.003
71. Choi D, Kumta PN (2006) Nanocrystalline TiN derived by a two-step halide approach for electrochemical capacitors. J Electrochem Soc 153(12):A2298. https://doi.org/10.1149/1.2359692
72. Ning W-W, Chen L-B, Wei W-F, Chen Y-J, Zhang X-Y (2020) $NiCoO_2$/NiCoP@Ni nanowire arrays: tunable composition and unique structure design for high-performance winding asymmetric hybrid supercapacitors. Rare Met 39(9):1034–1044. https://doi.org/10.1007/s12598-020-01374-9

Publisher's Note